CO 2 adsorption behaviour of nanosized CHA zeolites synthesised in the presence of barium or calcium cations

Aymeric Magisson, Edwin Clatworthy, Sajjad Ghojavand, Philippe Bazin, Valérie Ruaux, Eddy Dib, Svetlana Mintova

CO_2 adsorption behaviour of nanosized CHA zeolites synthesised in the presence of barium or calcium cations

Aymeric Magisson, Edwin B. Clatworthy, Sajjad Ghojavand, Philippe Bazin, Valérie Ruaux, Eddy Dib and Svetlana Mintova**

Laboratoire Catalyse et Spectrochimie (LCS), Normandie Université, ENSICAEN, UNICAEN, CNRS, 14050 Caen, France

Abstract

Alkaline-earth metal cations impact the rate of crystallisation and the adsorption of N_2 and CO_2 on nanosized chabazite zeolites. In this study, either calcium or barium was added to precursor mixtures containing alkali-metal cations (Na^+, K^+, Cs^+) to prepare chabazite (labelled Ca-CHA and Ba-CHA), and were compared to a reference sample (Ref-CHA) synthesized using exclusively Na^+, K^+, and Cs^+. Partial substitution of the Na^+ and the pore-blocking Cs^+ extra-framework cations was observed for Ca-CHA depending on the molar ratio of K_2O used in the synthesis, while a change to the amount of Na^+ cations only was observed for Ba-CHA. The type of alkaline-earth metal cation affects the crystallisation rate; slower in the presence of Ca^{2+} (10 h to full crystallinity) and similar rates in the presence of Ba^{2+} (4 h to full crystallinity); the crystallite size and morphology remained similar. The presence of Ca^{2+} or Ba^{2+} extra-framework cations leads to N_2 uptake values of 290 and 169 $mmol \cdot g^{-1}$ (−196 °C, 100 kPa), respectively, while at low CO_2 pressure (< 1 kPa, 25 °C), the physisorbed CO_2 capacity for Ref-CHA, Ca-CHA, and Ba-CHA zeolites is 0.63, 0.66, and 0.59 $mmol \cdot g^{-1}$, respectively. Interestingly, an opposite effect is observed for the amount of chemisorbed CO_2 species.

Keywords: *nanozeolite, chabazite, CO_2 adsorption, alkaline-earth metal cations, gas separation*

Zeolites are microporous solids possessing molecule-sized systems of channels and cages containing extra-framework cations and Brønsted acid sites. These characteristics confer remarkable properties which have led to their application in key adsorption, catalysis and cation exchange processes.[1] Over the last few decades there has been particular focus on the potential application of zeolites for the separation and capture of CO_2 in response to the increasing atmospheric concentration of greenhouse gases from anthropogenic sources.[2–4] Among the various solid adsorbents applicable for CO_2 separation, including metal organic frameworks[5], carbon-based adsorbents[6,7] and ionic liquids[8], zeolites possess an advantage of having tuneable capacity and selectivity towards CO_2 due to the relatively stronger interaction between CO_2 and the extra-

framework cations compared to other small molecules such as N_2 and CH_4.[9] The CO_2 adsorption behaviour of zeolites is influenced by the zeolite composition and its framework structure, directly related to the cationic environment and aluminium distribution of the zeolite.[10,11] The use of organic structure-directing agents (OSDAs) to synthesise specific zeolite topologies, compositions or particle morphologies is expensive due to the cost of the organic molecule which must be removed and destroyed by calcination after synthesis. Alternatively, zeolite syntheses using exclusively inorganic metal cations can direct the formation of different zeolite topologies and morphologies while lowering the number of synthetic steps.[12–14] Moreover, significantly higher surface area and reduced diffusion path length for guest molecules can be achieved by reducing the discrete particle size of the zeolite to the nanoscale, greatly improving their separation performance.[15]

The use of alkali-metal cations in the zeolite precursor mixture has been investigated extensively[16–20], but the impact of alkaline-earth metal cations and their influence as inorganic structure directing agents (ISDAs) has received less attention.[21–25] This is likely a consequence of their poor solubility in highly basic media compared to alkali-metal cations. An important consideration is that alkaline-earth metal cations have a higher charge density than alkali-metal cations while possessing similar ionic radii.[26] This makes them interesting ISDA candidates because fewer extra-framework cations are required to equilibrate the charge imbalance created by the presence of framework aluminium.[27] The pioneering work of Barrer and co-workers explored the hydrothermal chemistry of mixtures of silicon and aluminium precursors (Si sol and glasses, Al hydroxide and alumina gels) in the presence of either Ca^{2+}, Sr^{2+} or Ba^{2+} cations.[28–30] Their experiments yielded aluminosilicate products of varying purity and reproducibility, including chabazite zeolite in the presence of Sr^{2+}. Similarly, the hydrothermal treatment of kaolin with solutions containing $Ba(OH)_2$ was found to result in the formation of zeolites; chabazite was formed when using mixtures of KOH and $Ba(OH)_2$.[31,32] The influence of Sr^{2+} cations on the aluminium distribution in the chabazite framework and crystallisation rate was investigated recently, revealing

that the synthesis time could be reduced from weeks to hours.[33] Amongst the available literature, it has been reported that calcium- or barium-exchanged X-type faujasites and chabazites exhibit better adsorption capacity at very low CO_2 pressures,[34,35] yet a higher N_2 capacity was also observed for barium-exchanged X-type faujasites and chabazites at low pressures (<30 kPa).[26,36] In order to investigate the changes on both the synthesis and adsorption properties of nanozeolites prepared in the presence of alkaline-earth metal cations, we considered the chabazite framework because it exhibits a high adsorption capacity, and depending on the type of extra-framework cations present, a high selectivity towards CO_2 over CH_4 or N_2.[37] The CHA framework is described by a three-dimensional pore network containing super cages of (*t-cha*) connected by a double six ring (*t-hpr*) tiling. The diffusion of molecules through the cages is permitted by eight-membered rings (8MRs) which have a crystallographic free diameter of 3.8×3.8 Å.[38]

Here we describe the synthesis of two nanosized chabazite zeolites employing higher charge-density alkaline-earth metal cations (Ca^{2+}, Ba^{2+}) in the synthetic precursor mixture (Na^+, K^+ and Cs^+) previously reported. The N_2 and CO_2 adsorption behaviour of the Ca-, Ba- and Ref-CHA zeolites is investigated. An optimisation of the hydrothermal treatment (HT) was performed over different times to investigate the rate of crystallisation of the nanosized zeolites. The physical and chemical properties of the nanosized CHA zeolites were comprehensively characterised and the effects of the alkaline-earth metal cations were examined with reference to the nanosized CHA zeolite (Ref-CHA) prepared with Na^+, K^+ and Cs^+ extra-framework cations only.[39]

Material and Synthesis.

LUDOX AS-40 colloidal silica (SiO_2, Sigma-Aldrich, 40 wt% suspension), sodium aluminate ($NaAlO_2$, 50−56% Al_2O_3, 40−45% Na_2O Sigma-Aldrich) with an approximation of the minimum aluminium content of 50% and Na_2O of 43%, sodium hydroxide pellets (NaOH, Thermo Scientific, 98%), potassium hydroxide flakes (KOH, Sigma-Aldrich, 90%), caesium hydroxide solution

(CsOH, Sigma-Aldrich, 50%), calcium hydroxide powder ($Ca(OH)_2$, Sigma-Aldrich, 95%) and barium hydroxide powder ($Ba(OH)_2 \cdot 8H_2O$, Thermo Scientific, 98%) were used as received. All water used was MilliQ water from the Direct-8 ZR0Q008WW by Merck Millipore. The synthesis of CHA nanozeolite in the presence of alkaline-earth metals was performed in a sealed 60 mL polypropylene bottle. Sodium aluminate (0.594 g) was dissolved in MilliQ water (4.153 g) with rapid stirring. After solubilisation of the sodium aluminate, sodium hydroxide (1.704 g), potassium hydroxide (0.778 g), and a solution of caesium hydroxide (0.503 g) were added sequentially. This was then followed by the addition of either calcium or barium hydroxide (0.065 g or 0.152 g, respectively). After 2 h of stirring at room temperature, colloidal silica (10.0 g) was then added dropwise with rapid stirring. The alkali aluminosilicate colloidal suspension was then aged with rapid stirring for 7 days. The molar ratio of the initial Ca^{2+}-containing alkali aluminosilicate colloidal suspension is $0.20Cs_2O \cdot 1.5K_2O \cdot 6.0Na_2O \cdot 0.20CaO \cdot 16.0SiO_2 \cdot 0.70Al_2O_3 \cdot 140.0H_2O$, and the Ba^{2+}-containing alkali aluminosilicate colloidal suspension is $0.20Cs_2O \cdot 1.5K_2O \cdot 6.0Na_2O \cdot 0.20BaO \cdot 16.0SiO_2 \cdot 0.70Al_2O_3 \cdot 140.0H_2O$. A static hydrothermal treatment was performed for 2, 4 and 10 h in a preheated oven at 90 °C. The recovered material was washed with hot (90 °C) MilliQ water by centrifugation until the pH of the supernatant was neutral. The washed nanozeolite was then freeze-dried overnight using a Beta 1-8 LSCbasic from Martin Christ. Another synthesis of CHA nanozeolite was performed, identical in all aspects with the one described above except for a lowered amount of potassium hydroxide corresponding to an equivalent of 1.3 moles of K_2O. Sodium aluminate (0.594 g) was dissolved in MilliQ water (4.175 g) with rapid stirring. After solubilisation of the sodium aluminate, sodium hydroxide (1.704 g), potassium hydroxide (0.674 g), and a solution of caesium hydroxide (0.499 g) were added sequentially. This was then followed by the addition of either calcium or barium hydroxide (0.065 g or 0.152 g, respectively). The rest of the protocol is identical to the one described first.

Characterisation Techniques.

Powder X-Ray Diffraction (PXRD) patterns were collected on Anton Parr XRDynamic 500 diffractometer with a graphite monochromator in Bragg-Brentano configuration, Cu $K\alpha_1$ and $K\alpha_2$ radiation (λ = 1.5406, 1.5444 Å, 40 kV, 50 mA), and Pixos 2000 detector. The patterns were collected between 2θ of 5 and 60° with a step size of 0.03° and time per step of 492.606 s.

Inductively coupled plasma mass spectrometry (ICP-MS) measurements were performed on a 7900 ICP-MS from Agilent Technologies. 50 mg of sample was subjected to a digestive media (0.5 ml aqua regia at 1:3 HNO_3:HCl V/V, and 3 ml HF 40%) then heated to 110 °C for 1 hour before being neutralised with 2 g of boric acid and made up to 100 ml with milli-Q water.

Scanning Electron Microscopy (SEM) images were taken using a Tescan Mira I LMH under 30 kV. Energy Dispersive X-Ray (EDX) measurements were recorded using two Bruker XFLASH 6/30 EDX cameras.

Magic-angle spinning nuclear magnetic resonance (MAS NMR) spectra of ^{27}Al and ^{29}Si nuclei were recorded with a single pulse on a Bruker Avance 500 MHz (11.7 T) spectrometer using 4 mm outer diameter zirconia rotors with a MAS frequency of 12 kHz. Radiofrequency pulses of 2.2 µs (30° flip angle) were used for the acquisition of the ^{29}Si MAS NMR spectra with a recycle delay of 20 s, tetramethylsilane (TMS) was used as a chemical shift reference. Radiofrequency pulses of 1.25 µs (15° flip angle) were used for the acquisition of the ^{27}Al MAS NMR spectra with a recycle delay of 1 s, aluminium nitrate ($Al(NO_3)_3$) was used as a chemical shift reference.

N_2 adsorption and desorption isotherms were recorded at −196 °C on a Micromeritics 3Flex Surface Characterisation unit, and CO_2 adsorption isotherms were recorded at 0, 25 and 50 °C on a Micromeritics ASAP 2020 Surface Characterisation unit. The samples were outgassed under vacuum at 350 °C for 8 hours prior to the analysis. The specific surface area was calculated using the Brunauer-Emmett-Teller equation applying the Rouquerol criteria, the micropore volumes were determined using the non-local density functional theory (NLDFT) method.[40,41] Calculations of the

isosteric enthalpies of adsorption were performed using the Clausius–Clapeyron equation in VersaWin.

Thermogravimetric analysis (TGA) was performed using a STA 449 F3 Jupiter analyser, from 25 to 35 °C and held for 10 min with a flow of air (40 $mL \cdot min^{-1}$), from 35 to 800 °C at a heating rate of 10 $°C \cdot min^{-1}$, held at 800 °C for 10 min under air after reaching the target temperature, then cooled down to 25 °C at 20 $°C \cdot min^{-1}$.

In situ Fourier transform infrared (FTIR) spectroscopic measurements were performed using a self-supported pellet of a zeolite sample (approximately 20 mg with a diameter of 16 mm), recorded on a Thermo Scientific Nicolet iS50 FTIR spectrometer equipped with an MCT detector, at a spectral resolution of 4 cm^{-1} and 16 or 64 scans in absorption mode for the kinetic analysis and isotherm respectively. The experiments were performed in a "Carroucell" cell , attached to a vacuum system (greater than 10^{-5} mbar) that allows up to 12 different samples to be analysed with the same conditions.[42] The cell is equipped with a heating system to activate the samples at 350 °C prior to the measurements, at a rate of 2.7 $°C \cdot min^{-1}$, followed by heating at 350 °C for 4 h under high vacuum. All IR spectra related to CO_2 adsorption were recorded at room temperature. The molar absorption coefficients used to obtain both physisorption and chemisorption isotherms were 16 and 40 $cm \cdot \mu mol^{-1}$, respectively.[42] The quantitative amount of CO_2 adsorbed on the chabazite samples was determined using the peak area of the adsorbate, the molar absorption coefficient, and the thickness of the sample wafer.

Results and Discussion

The pure phase OSDA-free reference CHA nanozeolite was prepared using a mixture of inorganic alkali-metal cations where the Na^+ facilitates the solubilisation of silica and the stabilisation of the colloidal suspension, the K^+ promotes the formation of the secondary building units (SBUs), and the Cs^+ facilitates the stabilisation of the long-range crystalline order of the

framework.[39] The PXRD of the reference chabazite (Ref-CHA) was compared to a simulated phase of a fully crystalline chabazite (space group *R*−3*m*); no crystalline phases other than chabazite were observed (Figure 1). The Ca-CHA and Ba-CHA nanosized zeolite samples synthesised in the presence of alkaline-earth metal hydroxides (Ca^{2+} and Ba^{2+}) are compared with the reference nanosized zeolite Ref-CHA. A mixture of alkali-metal cations (Na^{+}, K^{+} and Cs^{+}) only is used to direct the synthesis of the Ref-CHA nanosized zeolite. Because of the similar ionic radii of Ca^{2+} and Na^{+}, and those of Ba^{2+} and K^{+}, we may reasonably expect a partial substitution of the sodium and potassium in the unit cell by calcium and barium cations, respectively.[26] Moreover, the choice of a low calcium or barium cation ratio in the precursor mixture is in consideration of the solubility limits of those two alkaline-earth metal cation hydroxides in aqueous solutions. To study the kinetics of the crystallisation of the Ca-CHA and Ba-CHA zeolites, the hydrothermal treatment at 90 °C was performed over three different time periods (2, 4, and 10 h). The samples were compared to the reference chabazite which achieves full crystallinity after 7 h of HT (Ref-CHA).[39] The PXRD patterns of the Ca-CHA and Ba-CHA are presented in Figure 1. After 2 h of HT the sample Ca-CHA remains amorphous indicated by the absence of Bragg peaks. After 4 h of HT the relative crystallinity is equal to 49% and reaches 100% after 10 h (Figure 1a, Table S1). The crystallinity was determined by comparing the integrated area of the peaks at 9.36 °, 12.8 °, 30.45 ° and 31.44 ° 2θ (Figure S1, Figure S2). In comparison, after 2 h of HT for the Ba-CHA sample, evidence of crystallisation is observed by the emergence of some weak Bragg peaks (Figure 1b). At 4 h of HT the PXRD pattern of the Ba-CHA indicates the completion of crystallisation. To verify that the Ba-CHA after 4 h was fully crystallised a sample was prepared with 10 h of HT. PXRD analysis revealed very little change in the intensity of the diffraction peaks indicating that 4 h of HT was enough to crystallise the nanosized chabazite in the presence of barium cations, with a relative crystallinity of 97% (Table S1, Figure 1).

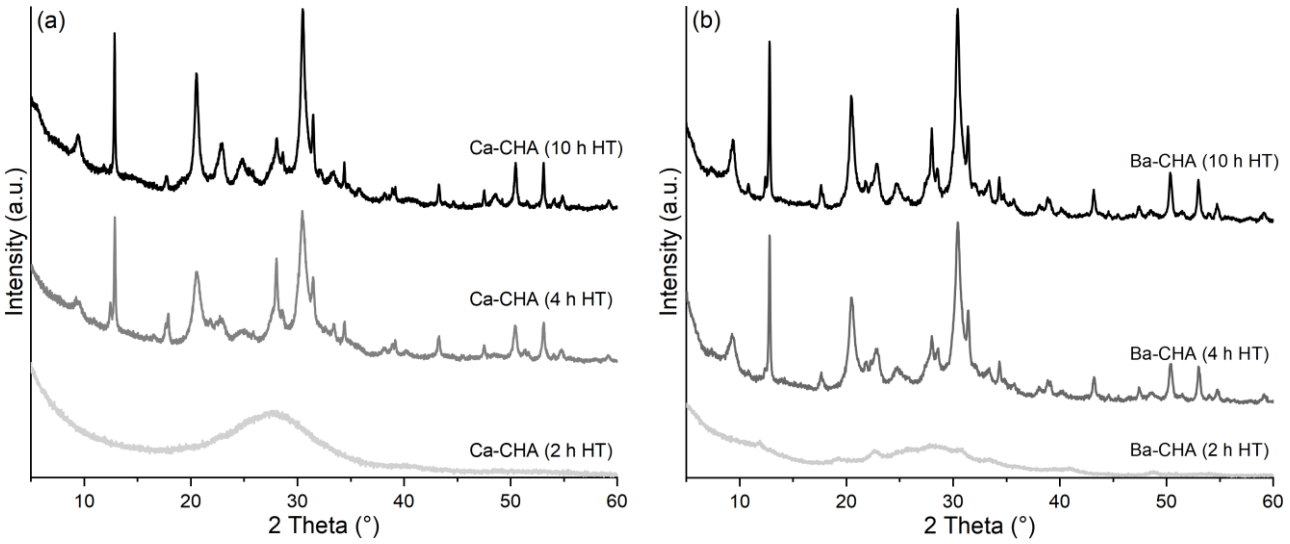

Figure 1. PXRD patterns of the nanosized chabazite zeolite samples (a) Ca-CHA, (b) Ba-CHA synthesized for 2, 4 and 10 h.

The reference sample (Ref-CHA) subjected to 4 h of HT was also synthesised to compare with

the reference zeolite prepared with 7 h of HT. The PXRD pattern of the reference zeolite obtained after 4 h of HT shows the exact same Bragg peaks with near identical crystallinity (95%) to the reference nanosized CHA zeolite after 7 h of HT (Figure S3). In comparison, a reference chabazite subjected to 2 h of HT treatment was found to be completely amorphous, similar to the Ca-CHA zeolite obtained after 2 h of HT. From the PXRD results, calcium cations clearly have an inhibiting effect on the rate of crystallisation while barium cations appear to slightly improve the rate of crystallisation of the nanosized chabazite. This is coherent with literature work realised on a low silica zeolite.[25] The morphology of the fully crystalline samples Ba-CHA (4 h HT) and Ca-CHA (10 h HT) were also evaluated and compared to the Ref-CHA nanosized chabazite by SEM (Figure 2). For all of the samples, identical discrete spherical particles 150–300 nm in diameter composed of

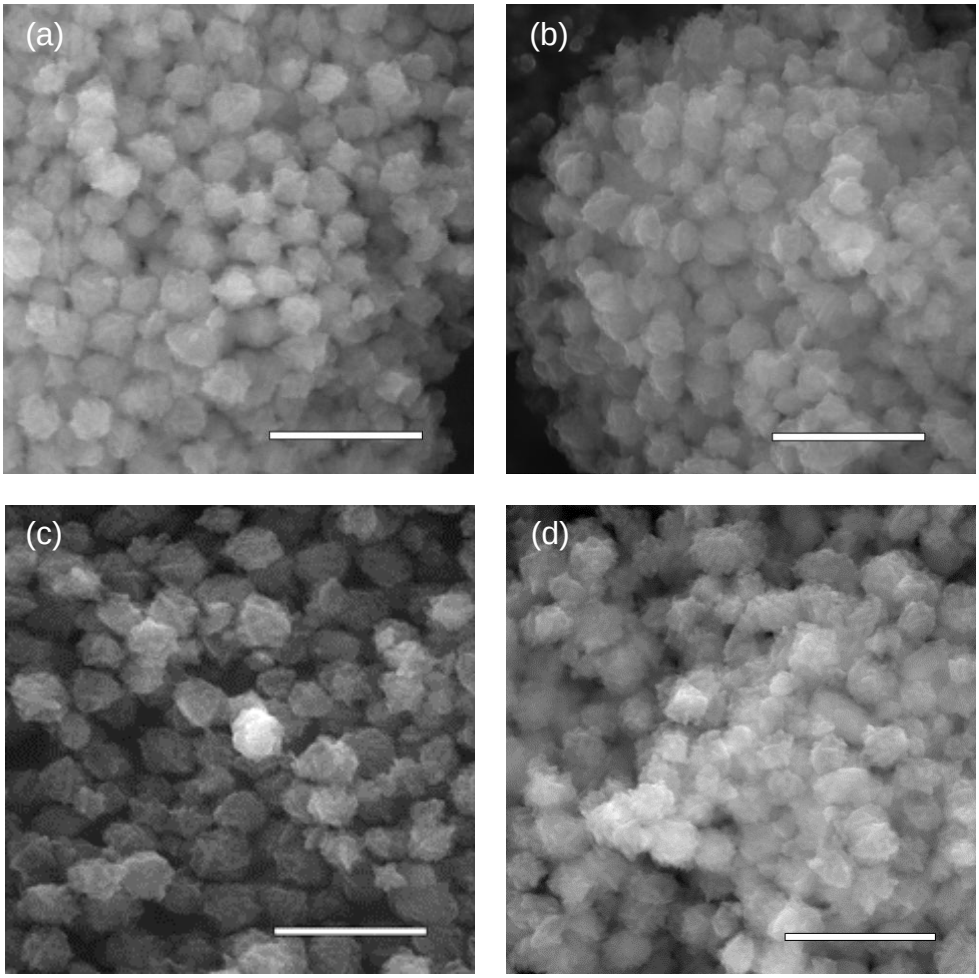

Figure 2. SEM images of (a) Ref-CHA (7 h HT) (b) Ref-CHA (4 h HT) (c) Ca-CHA (10 h) (d) Ba-CHA (4 h). Scale bar is 1 µm.

aggregated crystallites of 50–60 nm were observed. This is consistent with our previous observations investigating the effect of the ageing time of the alkali-metal aluminosilicate precursor suspension on the discrete particle size of CHA zeolites.[37,39,43] These results suggest that for the synthesis of nanozeolites conducted at high cation concentration and alkalinity, the effect of ageing time on the particle size remains largely unaffected by the addition of alkaline-earth metal cations employed at the concentrations used here. In comparison, the introduction of Ba^{2+} to the synthesis mixture of LTL has been shown to result in a reduction of the zeolite crystal size from 2.5 μm to 140 nm.[44] Additional images at different magnifications are presented in Figure S4.

The unit cell composition and the alkaline-earth metal extra-framework cation content of the nanosized chabazite samples were determined by ICP-MS and EDX (Table 1 and Table S2). The Ca-CHA sample has similar Na^+ and K^+ content to the reference zeolite, but a decrease in the Cs^+ content is observed. A negligible amount of precipitated $Ca(OH)_2$ was identified by EDX mapping of the Ca-CHA sample; the impurity persisted after extensive washings steps (Figure S5). This can be explained by the low solubility of calcium hydroxide in the precursor suspension. In the sample Ba-CHA some of the Na^+ cations were substituted for Ba^{2+}, while the amount of K^+ and Cs^+ cations remains unchanged compared to the Ref-CHA. In contrast to sample Ca-CHA, no precipitated $Ba(OH)_2$ in sample Ba-CHA was observed (Figure S5). The distribution and amount of cations of the Ca-CHA and Ba-CHA samples determined by ICP-MS and EDX analyses are similar. The

Table 1. Chemical composition of Ref-CHA, Ca-CHA and Ba-CHA determined by ICP-MS. *Due to the co-existence of $Ca(OH)_2$ precipitates the amount of Ca^{2+} cations present in the CHA unit cell was estimated.

Sample	Unit cell formula (ICP-MS)
Ref-CHA	$(Na_{2.5}K_{5.7}Cs_{3.1})Si_{24.7}Al_{11.3}O_{72}$
Ca-CHA*	$(Ca_{0.5x}Na_{3-x}K_{6.0}Cs_{2.7})Si_{24.3}Al_{11.7}O_{72}$
Ba-CHA	$(Ba_{0.5}Na_{1.6}K_{5.6}Cs_{3.2})Si_{24.6}Al_{11.4}O_{72}$

presence of alkaline-earth metal cations reduces the amount of sodium in both the Ca-CHA and Ba-CHA samples. This suggests, that for the mixed cation (Na^+, K^+, Cs^+) system employed here, Ca^{2+} and Ba^{2+} may play a similar primary role to Na^+, rather than the primary roles of K^+ or Cs^+, by

facilitating colloidal stability of the amorphous aluminosilicate particles prepared from monomeric Al and low molecular weight Si species. This may be rationalised by the similar or higher charge density of Na^+, Ca^{2+} and Ba^{2+} (24, 52 and 23 $C{\cdot}mm^{-3}$) cations compared to K^+ and Cs^+ (11 and 6 $C{\cdot}mm^{-3}$) cations, creating stronger interactions with negatively charged Al and Si species.[45] The observation of a similar K^+ cation content across all of the samples suggests that Ca^{2+} and Ba^{2+} cations do not act as inorganic directing agents in the synthesis of nanosized chabazite.

Due to the relatively low amount of alkaline-earth metal cations in the chabazite unit cell, two samples were prepared with a reduced amount of K_2O (1.3 moles equivalents) to determine whether the Ca^{2+} or Ba^{2+} loading could be increased. The decision to decrease the K_2O content, rather than the NaO_2 content, was made with consideration of the mixed cation (Na^+, K^+, Cs^+) system tolerating a lower K_2O ratio.[43] This permits maintaining the same ageing and hydrothermal treatment conditions while avoiding the formation of other structural phases. The PXRD results, elemental composition, thermogravimetric analysis and N_2 sorption isotherms are presented in the Supporting Information (Figures S6–S9 and Table S3). The PXRD patterns of the chabazites prepared with 1.3 K_2O in the presence of either Ca^{2+} or Ba^{2+} present identical peaks with slightly less intensity compared to the 1.5 K_2O samples. A small amount of phillipsite is present in the Ca^{2+}-containing chabazite, whereas the Ba^{2+}-containing chabazite exhibits reflections consistent with the chabazite structure only. The elemental composition of these two samples is similar to the fully crystalline samples described before, but with slightly lower amounts of extra-framework cations; the amount of alkaline-earth metal extra-framework cations is not increased. The results indicate that the synthesis of chabazite in the mixed cation (Cs^+, K^+, Na^+) system is not receptive towards the incorporation of alkaline-earth metal cations into the crystalline zeolite product, including when the amount of K^+ present in the synthesis is decreased. The elemental composition of the samples is confirmed by ICP-MS analysis.

The Si/Al ratios of the chabazite samples determined by ICP-MS, EDX and ^{29}Si MAS NMR are summarized in Table S4. The Si/Al ratio of the Ref-CHA based on ICP-MS and EDX is equal to 2.2 and 2.0, respectively which is consistent with our previous work, and similar to the value calculated based on the ^{29}Si MAS NMR using the Engelhardt equation.[39,46] For the Ca-CHA sample a slight increase in the Si/Al ratio was reported based by EDX while the Ba-CHA exhibited a similar Si/Al ratio to the Ref-CHA. The Si/Al ratio determined by ^{29}Si MAS NMR was consistent across all samples. The deconvoluted ^{29}Si MAS NMR spectra of the Ca-CHA and Ba-CHA in comparison to the Ref-CHA are presented in Figure 3. The ^{29}Si MAS NMR spectra for all chabazite samples present five peaks at −90, −94, −99, −105 and −110 ppm corresponding to a silicon coordinated as ($Si[AlO]_4$), ($Si[SiO][AlO]_3$), ($Si[SiO]_2[AlO]_2$), ($Si[SiO]_3[AlO]$) and ($Si[SiO]_4$) aluminium atoms respectively.[47,48] The overall broadening of all the Q^4 species and mainly the Q^4(nAl) where n is bigger than 2 in the Ca-CHA and Ba-CHA samples compared to the Ref-CHA, suggests an additional angular distortion in the framework. This is due to the partial substitution of monovalent cations by bivalent cations that are only stable when two or more aluminium are present in their surroundings. This effect is less pronounced for sample Ba-CHA, because of the higher electronegativity of Ca^{2+} compared to Ba^{2+} leading to a larger distortion of the negatively charged aluminium tetrahedra in the framework. ^{27}Al MAS NMR spectra of the Ref-CHA, Ca-CHA and Ba-CHA show a single peak around 57.9 ppm, indicating that all the aluminium atoms are tetrahedrally coordinated; no extra-framework aluminium is present (Figure S10).

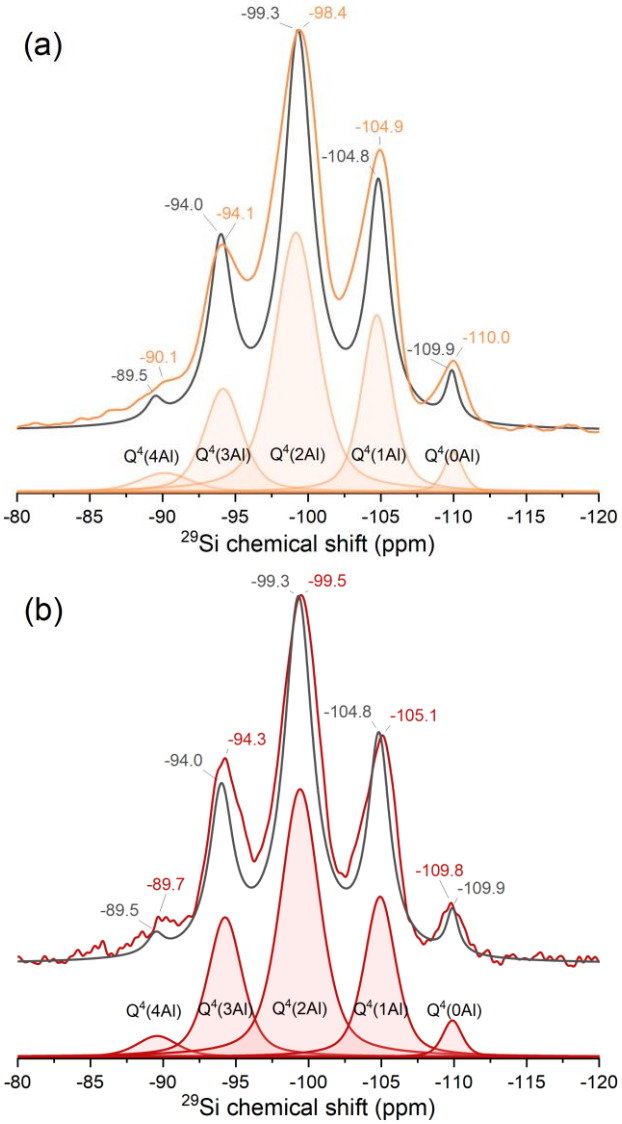

Figure 3: ^{29}Si MAS NMR spectra of samples (a) Ba-CHA (orange) and (b) Ca-CHA (red) in comparison to the Ref-

The dehydration of Ca-, Ba- and Ref-CHA nanosized zeolites was followed by thermogravimetric analysis (Figure 4). The majority of the mass loss occurs between 35 °C and 250 °C attributed to the removal of water adsorbed on the external surface and within the pores of the zeolite. Above 300 °C the mass loss is minimal and appears to recommence decreasing above 350 °C, corresponding to 1.3% for Ca-CHA and 0.9% for Ba-CHA but only 0.6% for the Ref-CHA. This is likely due to the condensation of silanols and is consistent with the difference in the total population of silanols of the three zeolite samples as determined by FTIR spectroscopy, *vide infra*. The total mass loss of all three samples at 300 °C is similar: 15.2%, 16.0% and 16.4% for the Ca-CHA, Ref-CHA and Ba-CHA, respectively.

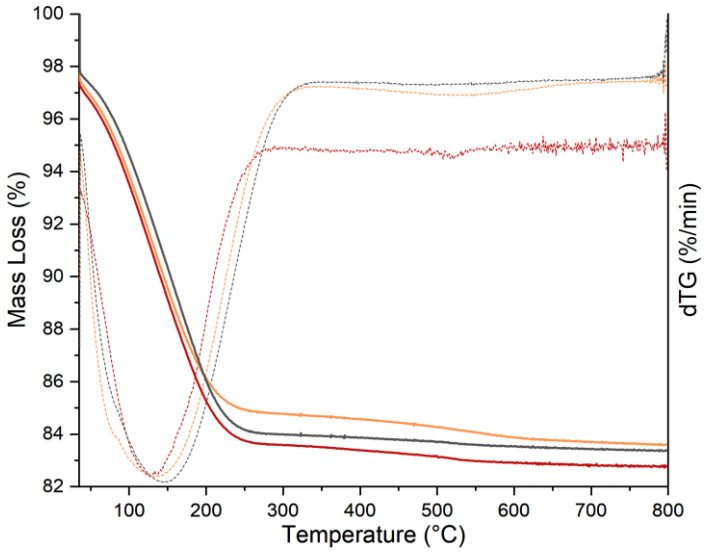

Figure 4. TG (solid) and dTG (dotted) curves of nanosized samples Ca-CHA (orange), Ba-CHA (red) and Ref-CHA (black)

Nitrogen sorption analysis was performed to investigate the effect of the presence of Ca^{2+} and Ba^{2+} on the textural properties of the nanosized CHA samples. Isotherms measured at −196 °C are presented in Figure 5 and the corresponding BET specific surface areas and the microporous volumes are summarised in Table S5. The influence of the different alkali-metal cations on the N_2 and CO_2 adsorption behaviour of nanosized and micron-sized CHA has been reported in earlier works.[35,49] The BET specific surface areas and micropore volumes for all of the chabazite nanozeolite samples presented here are low due to cation gating (trapdoor) behaviour. The increase of the BET specific surface area of the Ca-CHA (290 $m^2 \cdot g^{-1}$) relative to the Ref-CHA (136 $m^2 \cdot g^{-1}$) can be attributed to the reduced amount of Cs^+ acting as a door-keeper cation, thus N_2 molecules are less restricted at accessing the pores at −196 °C.[50,51] In comparison, the slight increase for the Ba-CHA (169 $m^2 \cdot g^{-1}$) may be due to the stronger interaction of N_2 with Ba^{2+}.[35] The BET specific surface areas of the Ca-CHA (172 $m^2 \cdot g^{-1}$) and Ba-CHA (155 $m^2 \cdot g^{-1}$) synthesised with 1.3 K_2O are slightly higher than that of the Ref-CHA made with 1.5 K_2O. The difference between the two Ca^{2+}-containing CHA can be explained by the changes in the Cs^+ extra-framework cation content, and the absence of $Ca(OH)_2$ in the 1.3 K_2O sample. The micropore volume of each of the samples is low; a minor increase is observed for the Ca-CHA sample synthesised in the presence of 1.5 K_2O ascribed to the lower extra-framework Cs^+ content.

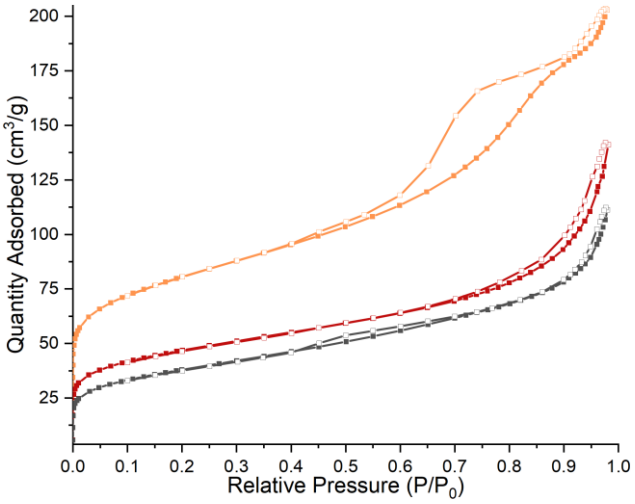

Figure 5. N_2 adsorption and desorption isotherms of the nanosized Ref-CHA (black), Ca-CHA (orange), and Ba-CHA (red) samples measured at −196 °C. Filled and empty squares represent the adsorption and desorption isotherms respectively.

To understand the influence of Ca^{2+} or Ba^{2+} extra-framework cations on the CO_2 adsorption behaviour of the nanosized CHA, volumetric adsorption and *in situ* FTIR analyses were performed. The CO_2 adsorption isotherms measured at 0, 25 and 50 °C are presented in Figure 6. The adsorption capacities are summarized in Table S6. The CO_2 adsorption behaviour of the nanosized CHA zeolite samples is broadly similar at 25 and 50 °C; some differences are observed for the isotherms recorded at 0 °C. The Ref-CHA exhibited the highest CO_2 capacity closely followed by the alkaline-earth metal containing CHA nanozeolites; the Ba-CHA synthesised with a 1.5 K_2O molar oxide ratio exhibited a notably lower adsorption capacity at 0 °C compared to the other samples. Similar behaviour has been observed for micron-sized Ba-containing CHA, however, the degree of Ba^{2+} exchange was much higher.[35]

The isosteric enthalpy of adsorption of CO_2 calculated using the Clausius–Clapeyron equation are presented in Figure S11. Across the entire coverage range the Ref-CHA, Ca-CHA ($1.5K_2O$) and Ba-CHA ($1.3K_2O$) exhibit similarly shaped curves, varying by up to ~4.1 kJ/mol at the highest coverage; the Ca-CHA ($1.5K_2O$) exhibits a more energetically uniform profile. Up to 1 mmol/g of coverage the Ca-CHA ($1.3K_2O$) and Ba-CHA ($1.5K_2O$) exhibit adsorption enthalpy values between 2.5 to 4.3 kJ/mol lower than the Ref-CHA before decreasing more sharply at higher coverage. The marked differences between the Ba-CHA samples may be due to the differences in the nature of the adsorption sites at 0 °C ascribed to differences in the Ba^{2+} site preferences.[52] For the Ca-containing

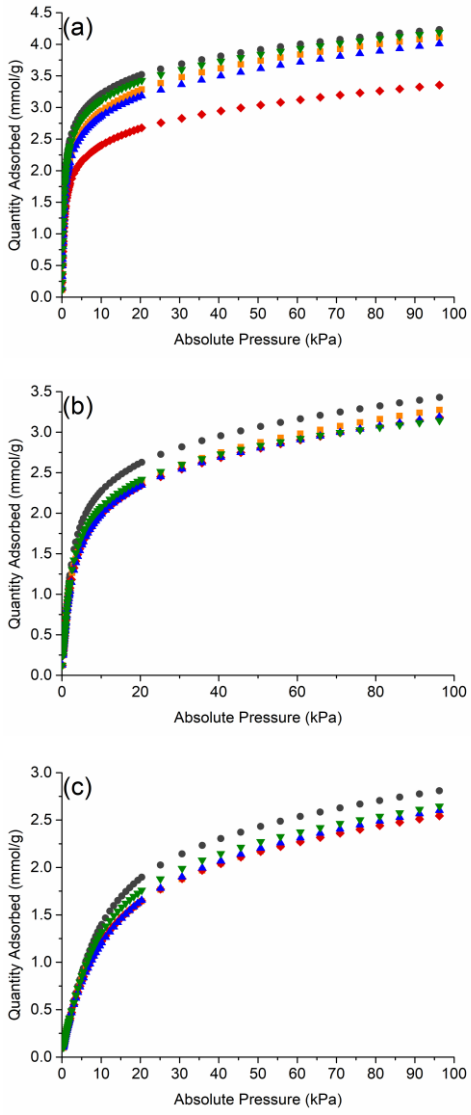

Figure 6: CO_2 adsorption isotherms recorded at (a) 0 °C, (b) 25 °C, and (c) 50 °C on the nanosized CHA zeolites: Ref-CHA (black circles), Ca-CHA $1.5K_2O$ (oranges squares), Ba-CHA $1.5K_2O$ (red diamonds), Ca-CHA $1.3K_2O$ (blue triangles), and Ba-CHA $1.3K_2O$ (green

nanosized CHA both samples exhibit similar adsorption enthalpy profiles offset by ~5.5–5.7 kJ/mol; the higher values for the Ca-CHA ($1.5K_2O$) are likely due to the presence of a relatively greater amount of higher charge density cations (Ca^{2+}, Na^+ and K^+) compared to Cs. Higher contents of Ca^{2+} and Ba^{2+} and determination of the cation locations by Rietveld analysis may provide further insight, but is beyond the scope of this study. For all of the CHA nanozeolite samples, it is expected that all of the Cs^+ extra-framework cations are located within the 8MRs, while Na^+ and Ca^{2+} are located within the *t-cha* cages near the double six ring prisms.[37,53] Since Ba^{2+} possesses a similar ionic radius to K^+ it is likely both cations fill positions near the double six ring prisms, and possibly within the 8MRs.[52] The CO_2 adsorption results suggest that the presence of alkaline-earth metal cations in the mixed (Cs^+, K^+, Na^+) cation CHA may reduce the adsorption enthalpy, but is dependent on their loading and presumably spatial arrangement.

The silanol region of FTIR spectra of activated Ca-CHA, Ba-CHA and Ref-CHA samples prior to CO_2 delivery is presented in Figure 7a; two major silanol peaks are observed. The O–H stretching frequency of the isolated or weakly bonded silanols in the range 3760–3700 cm^{-1} and the O–H stretching frequency of the moderately and strongly bonded silanols in the range 3700–3100 cm^{-1} are present.[54,55] The Ref-CHA sample has the lowest amount of silanols (464 $cm^{-1}\cdot g^{-1}$), determined by integrating a wide range of silanol sites across the entire range 3800–3100 cm^{-1}. Two bands at 3742 and 3726 cm^{-1} are clearly visible in the weakly H-bonded silanol region, while the H-bonded silanols of moderate strength are less intense for the Ref-CHA compared to those of the alkaline-earth metal cation containing chabazites.[56] The total concentration of silanol sites shows slight variations across the Ca-CHA, Ba-CHA and Ref-CHA samples (655, 632 and 644 $cm^{-1}\cdot g^{-1}$, respectively) which may be a reflection of the slight variations in extra-framework cation content.

The CO_2 adsorption on the samples was investigated by *in situ* FTIR spectroscopy in a custom cell allowing simultaneous analysis under identical conditions (pressure and temperature); the full

spectra are presented in the supporting information.[42] Two experiments were performed across a low pressure range of CO_2, between near-vacuum and 13.3 kPa. The physisorbed CO_2 species are quantitatively evaluated based on the gas-phase asymmetric stretching (ν_3) bands at 2346 cm^{-1} and 2280 cm^{-1} that correspond to the physisorbed $^{12}CO_2$ and $^{13}CO_2$ species, respectively.[57] The chemisorbed CO_2 is identified by the complex series of weak bands in the range 1750–1300 cm^{-1}.[56,58] After the first dose of CO_2, the Ref-CHA sample presents a pair of bands at 1683 and 1350 cm^{-1}, as well as weaker bands at 1720, 1654, 1380 and 1330 cm^{-1}. At 0.26 kPa, additional bands appear at 1641, 1560 and 1411 cm^{-1}. Above 0.80 kPa these bands become more distinct, including the appearance of a weak band at 1740 cm^{-1}. The bands in the FTIR spectra of samples Ca-CHA and Ba-CHA are similar to the Ref-CHA, however, the evolution behaviour and final intensities are different, indicating changes to the distribution of the coordination environments of the chemisorbed CO_2. For sample Ca-CHA, the intensity of the main chemisorption bands appears more evenly distributed. After the initial introduction of CO_2 (0.002 kPa), bands at 1683, 1653, 1609, 1381 and 1329 cm^{-1} are observed. Other bands at 1720 and 1351 cm^{-1} become more pronounced after delivery of 0.08 kPa CO_2, while the bands at 1402 cm^{-1} and 1560 cm^{-1} appear at 1.06 kPa CO_2; the bands at 1641 and 1740 cm^{-1} are less intense. The FTIR spectra of Ba-CHA are similar to those of the Ref-CHA. A pair of bands at 1681 and 1352 cm^{-1} along with bands at 1655, 1381, and 1314 cm^{-1} emerge after the first CO_2 delivery. After introducing 0.01 kPa of CO_2, a weak band at 1559 cm^{-1} appears. At 0.27 kPa CO_2 the band at 1742 cm^{-1} appears while the bands at 1720 and 1330 cm^{-1} are less intense. Above 2.27 kPa CO_2, the bands at 1408 and 1640 cm^{-1} become more intense.

Changes in the silanol region (3760–3675 cm^{-1}) of the IR spectra are observed as well. A decrease of the band at 3741 cm^{-1} and increase of bands at 3703 cm^{-1} ($\nu_3 + \nu_1$) and 3597 cm^{-1} ($\nu_3 + 2\nu_2$) are characteristic for weak interactions between the CO_2 and the hydroxyl groups of the activated zeolites (Figure S12 and S13). Above low pressure of CO_2 (>1 kPa), the $^{12}CO_2$ physisorption band

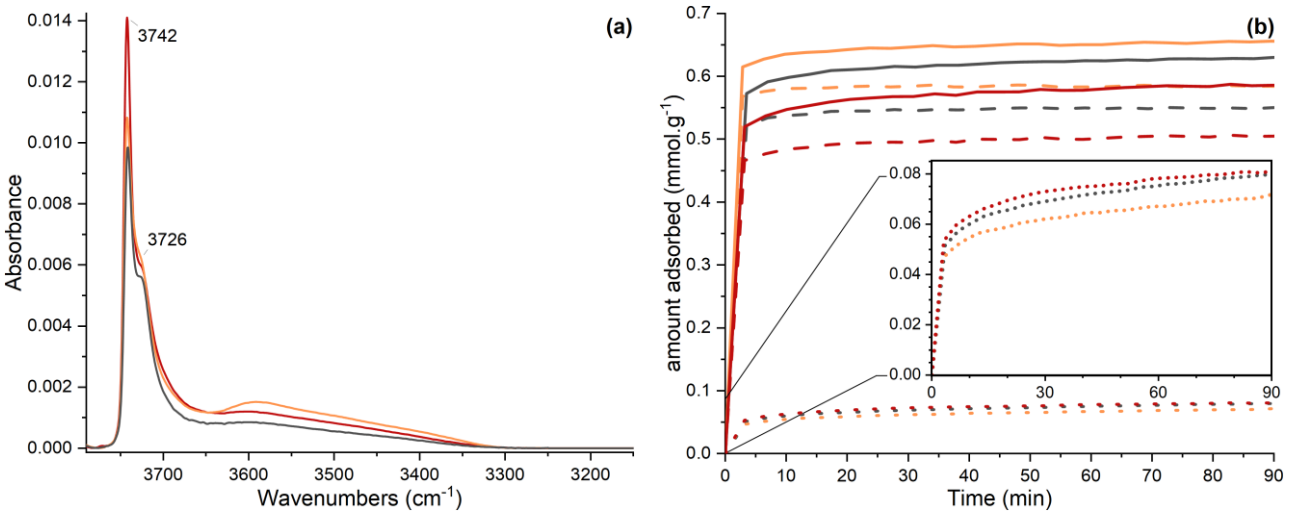

Figure 7. (a) FTIR spectra in the silanol region (3250-3800 cm^{-1}) of activated Ref-CHA (black), Ca-CHA (orange) and Ba-CHA (red), prior to CO_2 addition. (b) *In situ* FTIR CO_2 adsorption isotherms of nanosized samples Ref-CHA (black), Ca-CHA (orange) and Ba-CHA (red) recorded at 1 kPa CO_2: physisorbed (dashed line) and chemisorbed (dotted line) CO_2. The spectra of samples were recorded at 25 °C after activation at 250 °C.

is saturated and cannot be used for quantification. Consequently, the band of the $^{13}CO_2$ isotope with a natural abundance of 1.11% was used to determine the physisorbed CO_2.[59] The three isotherms of each sample, representing the physisorbed, chemisorbed, and total amount of adsorbed CO_2, measured at 25 °C are presented in Figure 7b. In the low-pressure range (0–1 kPa), samples Ca-CHA and Ba-CHA have very similar CO_2 uptake to the Ref-CHA zeolite. For the physisorbed CO_2 species, a clear trend is observed as follows Ca-CHA > Ref-CHA > Ba-CHA which may be ascribed to the higher charge density of Ca^{2+}. Interestingly an opposite trend is seen for the CO_2 chemisorbed species. At equilibrium after 90 minutes, the proportion of chemisorbed species over the total amount of CO_2 adsorbed corresponds to 10.9% for the Ca-CHA, 12.7% for the Ref-CHA and 13.7% for the Ba-CHA (Table S7), which is significantly higher than the ratio of CO_2 chemisorbed species over total adsorbed species at higher pressures. The value of the Ref-CHA is comparable to that of the as-prepared chabazite in previous work at near-identical pressure.[49] The high relative amount of chemisorbed species at low pressure is due to the coordination of CO_2 to strongly adsorbing sites.[60]

Conclusions

Alkaline-earth metal-containing zeolites have received less attention compared to their alkali-metal counterparts, despite their potential for various applications due to the tuneable adsorption behaviour. However, incorporating alkaline-earth metals into zeolites through direct synthesis methods remains challenging. Microscopic and PXRD analyses reveal that Ba-CHA nanocrystals synthesized for 4 hours exhibit higher crystallinity compared to reference nanosized chabazite (Ref-CHA), while maintaining the same size and morphology. This implies that only 4 hours of HT are needed to fully crystallise nanosized CHA in the presence of Ba^{2+}. On the other hand, the crystallisation rate of nanosized Ca-CHA is slower and require 10 hours of HT. Incorporating alkaline-earth metal cations into the aluminosilicate precursor mixture allows for the substitution of some Na^+ and Cs^+ cations, resulting in increased N_2 adsorption and higher specific BET surface area. While the crystallite size and particle morphology remain similar across all of the samples, the presence of alkaline-earth metal cations creates subtle differences to the silanol environments. Description of the CO_2 adsorption behaviour and isosteric enthalpy of adsorption is challenging due to the complexity of four different cations present in the chabazite crystals, however, the majority of the Ca- and Ba-containing samples exhibit high CO_2 adsorption capacity. An interesting effect of the alkaline-earth metal cations is observed in the nanosized chabazite samples under a dilute CO_2 atmosphere (<1 kPa). The Ca-CHA zeolite exhibits a higher amount of physisorbed CO_2 and a lower amount of carbonates, while the opposite effect is observed for the Ba-CHA sample. This study demonstrates that extra-framework alkaline-earth metal cations can be incorporated into the CHA zeolite using a direct synthesis approach, while also affecting the rate of zeolite crystallisation. The use of alkaline-earth metal cations for preparation of nanosized zeolites could be expanded to other structures with potential applications in gas separation processes.

Acknowledgements

Co-funded by the European Union (ERC, ZEOLIghT, 101054004). Views and opinions expressed are, however, those of the author(s) only and do not necessarily reflect those of the European Union or the European Research Council. Neither the European Union nor the granting authority can be held responsible for them. The authors acknowledge the support of the Centre for Zeolites and Nanoporous Materials, Label of Excellence, Normandy Region (CLEAR) and Marie Lozier for performing adsorption measurements.

References

1 W. Vermeiren, and J.-P. Gilson, *Topics in Catalysis*, **2009**, vol. 52, 1131–1161.
2 E. E. Knyazeva, A. V. Yakimov, O. V. Shutkina, S. V. Konnov, A. V. Panov, A. V. Kleimenov, D. O. Kondrashev, V. A. Golovachev, and I. I. Ivanova, *Petroleum Chemistry*, **2016**, vol. 56, 1168–1172.
3 S. Mukherjee, N. Sikdar, D. O'Nolan, D. M. Franz, V. Gascón, A. Kumar, N. Kumar, H. S. Scott, D. G. Madden, P. E. Kruger, B. Space, and M. J. Zaworotko, *Science Advances*, **2019**, vol. 5, eaax9171.
4 D. S. Sholl, and R. P. Lively, *Nature*, **2016**, vol. 532, 435–437.
5 X. Liu, X. Wang, and F. Kapteijn, *Chemical Reviews*, **2020**, vol. 120, 8303–8377.
6 A. E. Creamer, and B. Gao, *Environmental Science & Technology*, **2016**, vol. 50, 7276–7289.
7 S. Gadipelli, and Z. X. Guo, *Progress in Materials Science*, **2015**, vol. 69, 1–60.
8 T. U. Rashid, *Journal of Molecular Liquids*, **2021**, vol. 321, 114916.
9 S. Chatterjee, S. Jeevanandham, M. Mukherjee, D.-V. N. Vo, and V. Mishra, *Journal of Environmental Chemical Engineering*, **2021**, vol. 9, 105957.
10 M. Bui, C. S. Adjiman, A. Bardow, E. J. Anthony, A. Boston, S. Brown, P. S. Fennell, S. Fuss, A. Galindo, L. A. Hackett, J. P. Hallett, H. J. Herzog, G. Jackson, J. Kemper, S. Krevor, G. C. Maitland, M. Matuszewski, I. S. Metcalfe, C. Petit, G. Puxty, J. Reimer, D. M. Reiner, E. S. Rubin, S. A. Scott, N. Shah, B. Smit, J. P. M. Trusler, P. Webley, J. Wilcox, and N. Mac Dowell, *Energy & Environmental Science*, **2018**, vol. 11, 1062–1176.
11 E. Dib, E. B. Clatworthy, A. A. Paecklar, J. Grand, N. Barrier, and S. Mintova, *The Journal of Physical Chemistry C*, **2023**, vol. 127, 3–10.
12 Y. Mizuno, K. Miyake, S. Tanaka, N. Nishiyama, C. Fukuhara, and C. Y. Kong, *European Journal of Inorganic Chemistry*, **2021**, vol. 2021, 1405–1409.
13 A. Chawla, A. J. Mallette, R. Jain, N. Le, F. C. C. Robles Hernandez, and J. D. Rimer, SSRN Scholarly Paper at https://papers.ssrn.com/abstract=4078668 2022.
14 M. D. Oleksiak, and J. D. Rimer, *Reviews in Chemical Engineering*, **2014**, vol. 30, 1–49.
15 E. B. Clatworthy, S. Ghojavand, R. Guillet-Nicolas, J.-P. Gilson, P. L. Llewellyn, N. Nesterenko, and S. Mintova, *Chemical Engineering Journal*, **2023**, vol. 471, 144557.
16 S. Mintova, J.-P. Gilson, and V. Valtchev, *Nanoscale*, **2013**, vol. 5, 6693–6703.
17 E. B. Clatworthy, A. A. Paecklar, E. Dib, M. Debost, N. Barrier, P. Boullay, J.-P. Gilson, N. Nesterenko, and S. Mintova, *ACS Applied Energy Materials*, **2022**, vol. 5, 6032–6042.
18 M. M. Lozinska, E. L. Bruce, J. Mattock, R. G. Chitac, P. A. Cox, A. Turrina, and P. A. Wright, *Chemistry – A European Journal*, **2022**, vol. 28, e202201689.
19 X. Deng, P. Zhou, X. Yan, R. Xiong, H. Kou, and W. Luo, *Microporous and Mesoporous Materials*, **2021**, vol. 310, 110618.
20 A. Idris, U. Khalil, I. AbdulAziz, I. G. B. N. Makertihartha, Subagjo, M. Laniwati, A.-R. Al-Betar, R. R. Mukti, and O. Muraza, *Powder Technology*, **2019**, vol. 342, 992–997.
21 Y. Wang, Q. Wu, X. Meng, and F.-S. Xiao, *Engineering*, **2017**, vol. 3, 567–574.
22 Y. Liang, A. J. Jacobson, and J. D. Rimer, *Microporous and Mesoporous Materials*, **2023**, 112511.
23 J. C. Vega-Vila, A. Holkar, R. A. Arnold, D. P. Prentice, S. Dong, L. Tang, E. C. L. Plante, K. Ellison, A. Kumar, M. Bauchy, S. Srivastava, G. Sant, and D. Simonetti, *Reaction Chemistry & Engineering*, **2023**.
24 N. Rivera, S. Choi, C. Strepka, K. Mueller, N. Perdrial, J. Chorover, and P. A. O'Day, *American Mineralogist*, **2011**, vol. 96, 1809–1820.
25 A. Burton, and R. F. Lobo, *Microporous and Mesoporous Materials*, **1999**, vol. 33, 97–113.
26 R. D. Shannon, *Acta Crystallographica Section A*, **1976**, vol. 32, 751–767.
27 H. J. Choi, and S. B. Hong, *Chemical Engineering Journal*, **2022**, vol. 433, 133800.
28 R. M. Barrer, and P. J. Denny, *Journal of the Chemical Society*, **1961**, 983–1000.

29 R. M. Barrer, and D. J. Marshall, *Journal of the Chemical Society*, **1964**, 485–497.
30 R. M. Barrer, and D. J. Marshall, *Journal of the Chemical Society*, **1964**, 2296.
31 R. M. Barrer, R. Beaumont, and C. Collela, *Journal of the Chemical Society*, **1974**.
32 R. M. Barrer, and D. E. Mainwaring, *Journal of the Chemical Society, Dalton Transactions*, **1972**, 1259.
33 Y. Liang, A. J. Jacobson, and J. D. Rimer, *ACS Materials Letters*, **2021**, vol. 3, 187–192.
34 S. Liu, Y. Chen, B. Yue, C. Wang, B. Qin, Y. Chai, G. Wu, J. Li, X. Han, I. da- Silva, P. Manuel, S. J. Day, S. P. Thompson, N. Guan, S. Yang, and L. Li, *Chemistry – A European Journal*, **2022**, vol. 28.
35 J. Zhang, R. Singh, and P. A. Webley, *Microporous and Mesoporous Materials*, **2008**, vol. 111, 478–487.
36 S. E. Siporin, B. C. McClaine, and R. J. Davis, *Langmuir*, **2003**, vol. 19, 4707–4713.
37 M. Debost, P. B. Klar, N. Barrier, E. B. Clatworthy, J. Grand, F. Laine, P. Brázda, L. Palatinus, N. Nesterenko, P. Boullay, and S. Mintova, *Angewandte Chemie International Edition*, **2020**, vol. 59, 23491–23495.
38 L. S. Dent, and J. V. Smith, *Nature*, **1958**, vol. 181, 1794–1796.
39 S. Ghojavand, E. B. Clatworthy, A. Vicente, E. Dib, V. Ruaux, M. Debost, J. El Fallah, and S. Mintova, *Journal of Colloid and Interface Science*, **2021**, vol. 604, 350–357.
40 J. Rouquerol, P. Llewellyn, and F. Rouquerol, *Studies in Surface Science and Catalysis*, Elsevier, **2007**, 49–56.
41 S. Brunauer, P. H. Emmett, and E. Teller, *Journal of the American Chemical Society*, **1938**, vol. 60, 309–319.
42 V. Zholobenko, C. Freitas, M. Jendrlin, P. Bazin, A. Travert, and F. Thibault-Starzyk, *Journal of Catalysis*, **2020**, vol. 385, 52–60.
43 M. Debost, E. B. Clatworthy, J. Grand, N. Barrier, N. Nesterenko, J.-P. Gilson, P. Boullay, and S. Mintova, *Microporous and Mesoporous Materials*, **2023**, vol. 358, 112337.
44 O. Larlus, and V. P. Valtchev, *Chemistry of Materials*, **2004**, vol. 16, 3381–3389.
45 G. Rayner-Canham, and T. Overton, *Fifth edition* W. H. Freeman, **2009**.
46 G. Engelhardt, U. Lohse, V. Patzelová, M. Mägi, and E. Lippmaa, *Zeolites*, **1983**, vol. 3, 233–238.
47 S. Ghojavand, E. Dib, B. Riodent, A. Magisson, V. Ruaux, and S. Mintova, *Advanced Sustainable Systems*, **2023**, 2200480.
48 S. Ghojavand, E. Dib, J. Rey, A. Daouli, E. B. Clatworthy, P. Bazin, V. Ruaux, M. Badawi, and S. Mintova, *Communications Chemistry*, **2023**, vol. 6, 1–8.
49 S. Ghojavand, B. Coasne, E. B. Clatworthy, R. Guillet-Nicolas, P. Bazin, M. Desmurs, L. Jacobo Aguilera, V. Ruaux, and S. Mintova, *ACS Applied Nano Materials*, **2022**.
50 J. Shang, G. Li, R. Singh, P. Xiao, J. Z. Liu, and P. A. Webley, *The Journal of Physical Chemistry C*, **2013**, vol. 117, 12841–12847.
51 J. Shang, G. Li, R. Singh, Q. Gu, K. M. Nairn, T. J. Bastow, N. Medhekar, C. M. Doherty, A. J. Hill, J. Z. Liu, and P. A. Webley, *Journal of the American Chemical Society*, **2012**, vol. 134, 19246–19253.
52 M. Calligaris, and G. Nardin, *Zeolites*, **1982**, vol. 2, 200–204.
53 W. J. Mortier, J. J. Pluth, and J. V. Smith, *Materials Research Bulletin*, **1977**, vol. 12, 97–102.
54 E. Dib, I. M. Costa, G. N. Vayssilov, H. A. Aleksandrov, and S. Mintova, *Journal of Materials Chemistry A*, **2021**, vol. 9, 27347–27352.
55 F. Dubray, E. Dib, I. Medeiros-Costa, C. Aquino, D. Minoux, S. Van Daele, N. Nesterenko, J.-P. Gilson, and S. Mintova, *Inorganic Chemistry Frontiers*, **2022**, vol. 9, 1125–1133.
56 T. Montanari, and G. Busca, *Vibrational Spectroscopy*, **2008**, vol. 46, 45–51.
57 J. C. Lavalley, *Catalysis Today*, **1996**, vol. 27, 377–401.
58 R. W. Stevens, R. V. Siriwardane, and J. Logan, *Energy & Fuels*, **2008**, vol. 22, 3070–3079.
59 Q.-L. Zhang, C. T. L., and W.-J. Li, *Chinese Science Bulletin*, **1990**, vol. 35, 290–296.
60 A. Zukal, C. O. Arean, M. R. Delgado, P. Nachtigall, A. Pulido, J. Mayerová, and J. Čejka, *Microporous and Mesoporous Materials*, **2011**, vol. 146, 97–105.

Table of Contents File

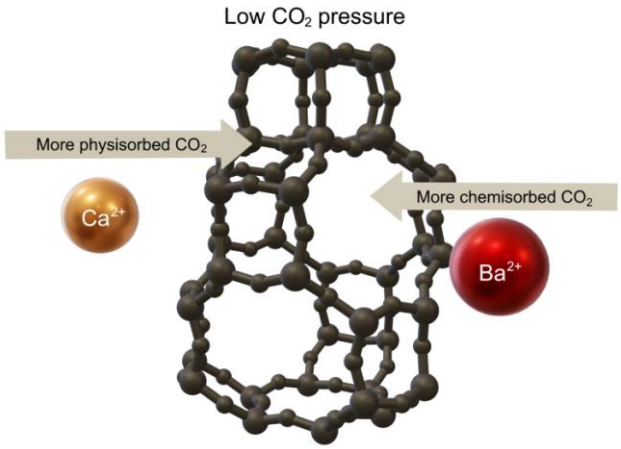
Low CO_2 pressure
More physisorbed CO_2
More chemisorbed CO_2
Ca^{2+}
Ba^{2+}